



Unraveling circular polarimetric images of magnetically arrested accretion flows near event horizon of a black hole

M. Mościbrodzka¹ , ¹★ A. Janiuk² and M. De Laurentis^{3,4}

¹Department of Astrophysics/IMAPP, Radboud University, PO Box 9010, NL-6500 GL Nijmegen, the Netherlands

²Center for Theoretical Physics PAS, Al. Lotnikow 32/46, PL-02-668 Warsaw, Poland

³Dipartimento di Fisica ‘E. Pancini’, Università di Napoli ‘Federico II’, Via Cinthia, I-80126, Napoli, Italy

⁴INFN Sezione di Napoli, Via Cinthia, I-80126, Napoli, Italy

Accepted 2021 September 23. Received 2021 September 23; in original form 2021 April 7

ABSTRACT

Magnetically arrested accretion flows are thought to fuel some of the supermassive black holes and to power their relativistic jets. We calculate and study a time sequence of linear and circular polarimetric images of numerical, high resolution, and long-duration simulations of magnetically dominated flows to investigate observational signatures of strong magnetic fields near the event horizon of a non-rotating black hole. We find that the magnitude of resolved linear and circular polarizations is rather sensitive to the assumption of the coupling of electron and ions in the accretion flow. Models with cooler electrons have higher Faraday rotation and conversion depths, which result in scrambled linear polarization and enhanced circular polarization. In those high Faraday thickness cases, the circular polarization is particularly sensitive to dynamics of toroidal-radial magnetic fields in the accretion flows. The models with high Faraday thickness are characterized by nearly constant handedness of circular polarization, consistent with observations of some accreting black holes. We also find that the emission region produced by light, which is lensed around the black hole, shows inversion of circular polarization handedness with respect to the handedness of the circular polarization of the entire emission region. Such polarity inversions are unique to near horizon emission.

Key words: black hole physics – MHD – polarization – radiative transfer – relativistic processes.

1 INTRODUCTION

Low Luminosity Active Galactic Nuclei (LLAGN) are believed to be powered by magnetized radiatively inefficient accretion flows (MRIAFs) on to a supermassive black hole (e.g. Yuan & Narayan 2014). One of the main uncertainties in these type of accretion flows is their magnetic field strength, geometry, and dynamics, which span from turbulent to organized and reconnecting (e.g. Beckwith, Hawley & Krolik 2008; Ressler et al. 2020). Magnetic fields determine the accretion flow dynamics and likely play a leading role in the jet formation process (Blandford & Znajek 1977; Blandford & Payne 1982). Hence, understanding their observational signatures close to the central black hole is a key to find connections between jet, accretion flow, and the black hole itself.

The geometry of magnetic fields around black holes is best studied in terms of linear and circular polarization of the emitted synchrotron light, the primary cooling process of MRIAFs. However, extracting information about the underlying field geometry from light polarization is not straightforward. First, the polarization signal from near black hole event horizon zone is distorted by gravitational lensing and Doppler boosting effects (Connors, Piran & Stark 1980; Ishihara, Takahashi & Tomimatsu 1988; Himwich et al. 2020). Secondly, the polarization signal can be affected by plasma effects changing polarization when light propagates through it. In Mościbrodzka et al. (2017; see also Jiménez-Rosales & Dexter 2018), we have shown

the Faraday effects present internally in MRIAFs are able to severely modify the linear polarization of synchrotron light. While these internal Faraday effects strongly depend on the assumed model for plasma and field configuration in the LLAGN core, linear polarization can be also subject to additional modifications by Faraday screens, which are physically displaced from the LLAGN core (in fact such external Faraday screen effect is often used to infer mass accretion rate towards LLAGNs; see e.g. Marrone et al. 2007; Kuo et al. 2014). While linear polarization can be sensitive to the details of magnetic field and plasma configuration on large span of distances from the central black hole, the circular polarization is sensitive to near-horizon processes only. Although usually weaker (as shown in this work), circular polarization of synchrotron light may become an important probe of the near horizon plasma and magnetic field configuration and dynamics. Hence, the focus of this work is mostly on circular polarization.

The circular polarization is detected in radio observations of many AGN jets (e.g. Wardle et al. 1998, Homan & Lister 2006). It has been reported that circular polarization magnitude in those brighter sources might correlate with their spectral indices (Rayner, Norris & Sault 2000). The circular polarization is also found in couple of LLAGN sources (the notable examples are: Sgr A*, Bower, Falcke & Backer 1999, Bower, Falcke & Mellon 2002, Brunthaler, Bower & Falcke 2006, Muñoz et al. 2012, M 81* and recently also in M87, Goddi et al. 2021). Interestingly, the handedness of circular polarization in many of these accreting supermassive black holes remains constant over the years and even decades (Homan & Wardle 1999, Bower et al. 2002, Bower et al. 2018). It has been proposed that

* E-mail: m.moscibrodzka@astro.ru.nl

such long-term stability of circular polarization sign could be a results of: (i) the presence of stable global magnetic field component in the accretion flow system (e.g. Beckert & Falcke 2002); (ii) direction of rotation in an accreting system (e.g. Enßlin 2003).

In the present article, we analyse polarimetric properties of realistic MRIAFs models obtained by combining high resolution, large domain, 3D general relativistic magnetohydrodynamics (3D GRMHD) simulations with fully polarized radiative transfer model. Our 3D GRMHD runs are evolved for relatively long times (up to about $t_f \sim 50\,000\,M$), which enable us to study long-term stability of the magnetic fields and associated polarization of the models. Our goal is to find the physical origin of the polarization signal and its characteristics. We introduce a diagnostic method which tracks, along the light paths, the components of the radiative transfer equation. The diagnostics allows us to identify the location and processes responsible for the observed model linear and circular polarization and, hence, helps to associate the emission polarization with, e.g. the underlying magnetic field geometry. The models chosen for the study are magnetically arrested disks (hereafter MAD; e.g. Narayan, Igumenshchev & Abramowicz 2003; Proga & Begelman 2003; McKinney, Tchekhovskoy & Blandford 2012). We study three slightly different numerical realizations of MADs. Mock observations are created at observer's frequency, where the emission from black hole event horizon scale, where jet base and disc are connected, is visible. Our theoretical study is limited to near face-on observations corresponding to the viewing angle of LLAGN in M87 galaxy. M87 galaxy core is currently one of the most promising astrophysical sources where the details of the black hole-jet-disc connection theories can be quantitatively tested (Broderick & Loeb 2009; Dexter, McKinney & Agol 2012; Mościbrodzka, Falcke & Shiokawa 2016; Mościbrodzka et al. 2017; Chael, Narayan & Johnson 2019; Event Horizon Telescope Collaboration 2019a,b). Recently, near-horizon linear polarimetric images of M87 have been published (Event Horizon Telescope Collaboration 2021a,b). The new images allow us to put much tighter constraints on our model free parameters.

The article is structured as follows. In Section 2, we present our methodology for modelling and investigating polarimetric signal of numerical models of MRIAFs. In Section 3, we present polarimetric maps of MAD flows and investigate the origin of the light linear and circular polarizations. In Section 4, we briefly discuss the new results and conclude.

2 METHODOLOGY

2.1 Magnetically arrested accretion flow models

We use the general relativistic magneto-hydrodynamic code, HARM (Gammie, McKinney & Tóth 2003; Noble et al. 2006; Sapountzis & Janiuk 2019), with a fixed background Kerr metric, i.e. neglecting the effects of self gravity and the black hole spin changes (cf. Janiuk, Sukova & Palit 2018). The numerical scheme is based on GRMHD equations where the energy-momentum tensor is contributed by the gas and electromagnetic fields. The code solves the fluid evolution based on continuity and momentum conservation equations.

The HARM code performs the integration in Modified Kerr-Schild coordinates: $(t, x^{(1)}, x^{(2)}, \phi)$. The assumed grid is exponential in radius, while in the polar direction, the cells are concentrated more on the mid-plane. Moreover, cylindric coordinates are used inside the radius $R_{\text{cyl}} = 3.5$ and inside the angle $\theta_{\text{cyl}} = -1 + 1/N_2$, to resolve better the regions closest to the black hole horizon and the polar axis. The inner and outer radius are set to $R_{\text{in}} = 0.87(1 + \sqrt{1 - a^2})$, and $R_{\text{out}} = 10^5\,M$, where $M \equiv GM/c^2$ is a length unit. The progressively

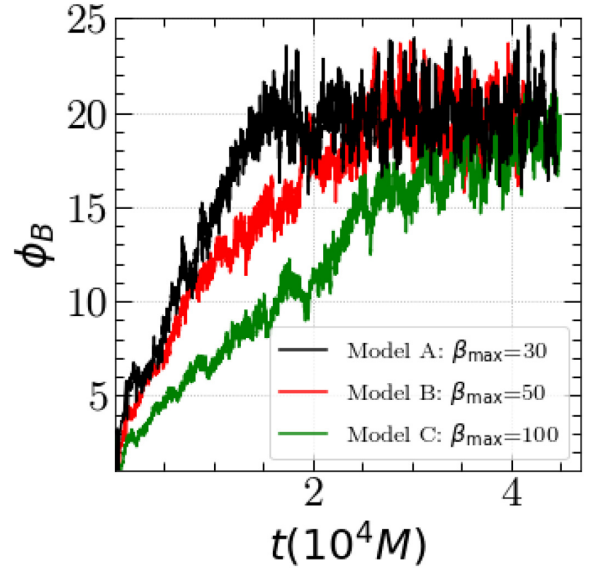


Figure 1. Normalized magnetic field flux, $\phi_B = \Phi_B / \sqrt{M}$, at the horizon as a function of time in three realizations of MAD model.

sparser grid starts at $R_{\text{br}} = 400$, with $x_i^{(1)} = x_{i-1}^{(1)} + 0.5 \times \delta x$, where $\delta x = \log(R_{\text{out}} - 2)^{1/4} + \log(R_{\text{br}})$. Our grid resolution (N_1, N_2, N_3) in the (r, θ, ϕ) directions depends on the model (see paragraphs below).

The initial configuration of the flow is based on the analytic solution of a constant specific angular momentum, in a steady state configuration of a pressure-supported ideal fluid in the Kerr black hole potential (Fishbone & Moncrief 1976). The initial torus embeds a poloidal magnetic field, prescribed with the vector potential of

$$A_\phi = \left(\frac{\bar{\rho}}{\rho_{\text{max}}} - \rho_0 \right) r^5 \quad (1)$$

where $\bar{\rho}$ is the density in the torus averaged over two neighbouring cells, and ρ_{max} is the density maximum, and we use offset of $\rho_0 = 0.2$. The factor of r^5 ensures that higher magnetic flux will be brought on to the black hole horizon from larger distances, as the evolution proceeds. Other spatial components of the initial vector potential are zero, $A_r = A_\theta = 0$, hence the initial magnetic field vector will have only B_r and B_θ components. The plasma β -parameter is defined as the ratio of the fluid's thermal to the magnetic pressure, $\beta \equiv p_g/p_{\text{mag}}$. We normalize the magnetic field in the torus to have $\beta_{\text{max}} = (\gamma - 1)u_{\text{max}}/(b_{\text{max}}^2/2)$, where u_{max} is the internal energy at the torus pressure maximum radius. In our models, the adiabatic index of $\gamma = 4/3$ is used.

The magnetically arrested flows are supposed to accrete on to black hole when overpassing the magnetic barriers. Therefore, in order to introduce a non-axisymmetric perturbation and allow the generation of azimuthal modes, we impose an initial perturbation of internal energy. It is given by $u = u_0(0.95 + 0.1C)$, where C is a random number generated in the range $(0, 1)$. This perturbation on the order of less than 5 per cent is typically used in other 3D simulations of weakly magnetized flows (see Mizuta et al. 2018).

We carry out three high resolution simulations of MAD accretion flow on to Schwarzschild black hole. Starting conditions differ by β_{max} parameter. Model A, B, and C starts with $\beta_{\text{max}} = 30, 50$, and 100, respectively. The resolutions (N_1, N_2, N_3) are (288, 256, 256), (576, 512, 256), and (576, 256, 256) in model A, B, and C, respectively. The GRMHD simulations A/C are evolved for $\sim 45\,000\,M$ and simulation B for $41\,000\,M$, where $M \equiv GM/c^3$ is a time unit. In Fig. 1, we show time evolution of the magnetic field flux

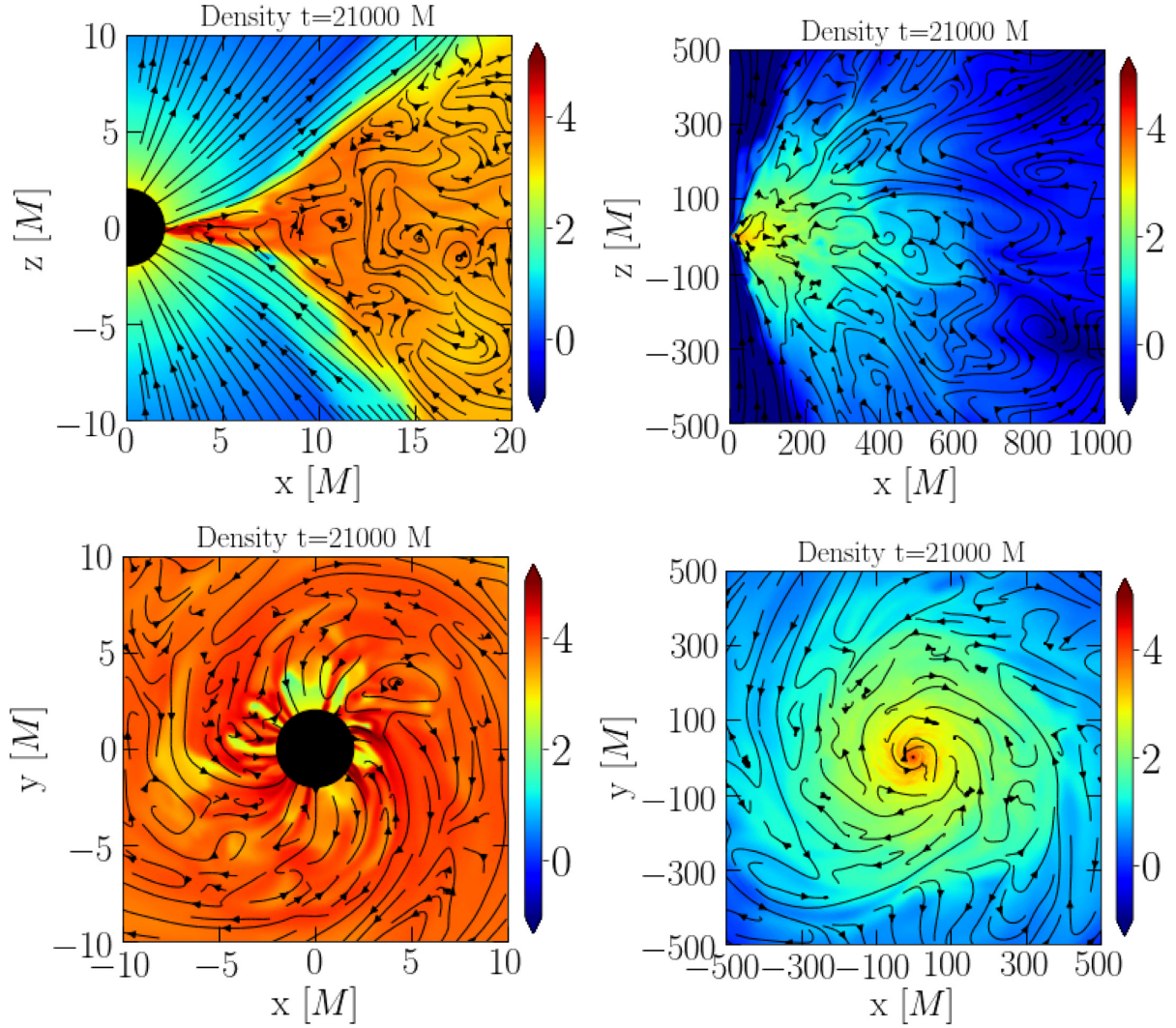


Figure 2. Maps of the density (in arbitrary units), in the polar plane XZ (top row) and in the equatorial plane XY (bottom row) of model A. Left-hand and right-hand panels show the same model on different scales. The colour maps are in logarithmic scale and are taken at times denoted in the plots ($t \sim 21\,000\,M$). Black contours follow magnetic field lines projected on to x-y and x-z Cartesian coordinates.

through the horizon in our three realizations of MAD model. Note that our initial normalization of magnetic fields affected the time at which the MAD state is reached. For smallest β_{\max} , in model A, the normalized magnetic flux on the black hole horizon as time $t = 21\,000\,M$ was equal to ~ 20.9 , while for models B and C it was about ~ 16.0 and ~ 10.7 , respectively. At the end of these simulations, already all models resulted in $\phi_B \approx 16 - 21$, which we consider as the magnetically arrested mode (largest instantaneous value was reached in model B). On the other hand, the accretion rate at the black hole, measured at time $t = 21\,000\,M$, was largest for model C, which is least magnetized. The time-averaged accretion rate, though, was maximal for model A, and it was 0.981 (in code units), while the time averaged accretion rates of models B and C were equal to 0.843 and 0.587 , respectively. In model A, the MAD state is reached at $t \approx 15\,000\,M$ at which the magnetic field flux at the horizon saturates. In Fig. 2, we show model A density maps overplotted with magnetic field lines contours at $t = 21\,000\,M$. Within inner-most stable orbit the accretion proceeds in form of thin streams (fingers) of nearly radially falling matter that is able to overpass the pressure of the magnetosphere.

2.2 Radiative transfer and electron heating models

Polarimetric images of the GRMHD models are computed by post-processing the simulations fluid variables with the polarized relativistic radiative transfer code *ipole*¹ (Mościbrodzka & Gammie 2018). We scale the GRMHD simulations to black hole in M87 galaxy centre, which we use here as an example of astrophysical source, and we calculate polarimetric images at frequency $f = 230\,\text{GHz}$ to focus the analysis on emission properties on the near horizon scales. All images are computed for two viewing angles $i = 20, 160\,\text{deg}$ corresponding to the putative viewing angles of M87 core.

The GRMHD simulations themselves do not follow the evolution of radiating electrons temperatures which are needed to calculate synchrotron emission. For the considered plasma number densities ($n_e \approx 10^2 - 10^5\,\text{cm}^{-3}$), we can assume that electrons can be thermally de-coupled from ions and electron distribution function is controlled by other collisionless plasma processes. Following the approach introduced by Mościbrodzka et al. (2016), the collective plasma

¹www.github.com/moscibrodzka/ipole

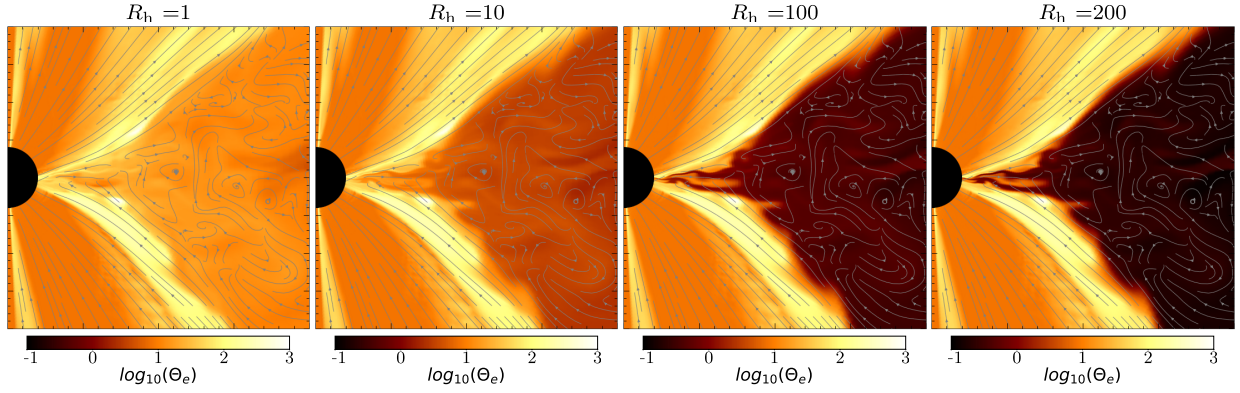


Figure 3. Impact of R_h parameter on electron temperature in MAD simulation A. Model snapshot at $t = 21\,150\,M$ within $20 \times 20\,M$ is shown and the black hole is marked with the black circle. The grey contours mark magnetic fields lines projected from coordinate basis (modified Kerr–Schield coordinates) to x-z plane in Cartesian coordinates.

effects heating electrons are described by parameter R_h , which sets the ratio of ion to electron temperatures in the high- β plasma regions (where plasma $\beta \equiv p_g/p_{\text{mag}}$). The electron temperature is calculated from expression:

$$T_e = T_i \left(\frac{R_h \beta^2}{1 + \beta^2} + \frac{1}{1 + \beta^2} \right)^{-1}, \quad (2)$$

where the ion temperature, T_i , is calculated from simulation gas pressure assuming ideal gas law. As shown in Fig. 3, by increasing R_h the decoupling of electron and ions in the weakly magnetized plasma (higher β regions) is stronger and electrons may become sub-relativistic in these regions. In these models, the emission from the places where the magnetic fields are relatively stronger and well organized is expected to be more prominent. In Mościbrodzka et al. (2017), we have investigated linear polarization of the same emission models for M87 core but using non-MAD simulations. Here, we extend our studies to MAD models and circular polarization.

In our emission modelling we use so called fast-light approximation where we post-process each simulation dump file separately as if light had infinite speed. In Appendix A, we explicitly show that this approximation holds very well for simulations of unpolarized/polarized radiative transfer through an accreting torus.

2.3 Polarization diagnostics

In relativistic plasma, the circular polarization can be produced in two ways: via intrinsic emission² and via Faraday conversion. In our simulations, both effects are contributing to final circular polarimetric maps and Faraday conversion becomes increasingly important with increasing R_h parameter. Because of the Faraday conversion (of linear to circular polarization) circular polarization has to be analysed simultaneously with linear polarization. Apart of total intensity \mathcal{I} and fractional circular polarization ($v \equiv V/I$), we also examine maps of linear polarization angles ($EVPA \equiv 0.5 \arctan(Q + iU)$) and fractional linear polarization ($|m| \equiv \sqrt{Q^2 + U^2}/I$). We also define image net linear and circular

polarizations as $|m|_{\text{net}} \equiv \sqrt{(\sum_{i,j} Q_{i,j})^2 + (\sum_{i,j} U_{i,j})^2} / (\sum_{i,j} I_{i,j})$ and $v_{\text{net}} \equiv (\sum_{i,j} V_{i,j}) / (\sum_{i,j} I_{i,j})$, where sums are over all image pixels.

The origin of linear and circular polarization in the polarization maps can be studied using a simplified but more formal approach than quantitative and qualitative description of polarization maps. The presented approach is most useful for investigating time variability of the polarimetric images. In the fluid rest-frame, the equations for relativistic polarized radiative transfer (see e.g, equation 19 in Mościbrodzka & Gammie 2018 and notice that our fully covariant polarized radiative transfer equations accounts for polarization vector parallel transport outside of the fluid frame) can be recast into a form in which they have simple geometrical interpretation. In an analogy to Landi Degl’Innocenti & Landolfi (2004; chapter 5.6), the relativistic polarized radiative transfer equations can be written down separately for invariant total intensity I ($I \equiv I_v/v^3$) and fractional polarization three-vector $\vec{p} \equiv (Q/I, U/I, V/I)$ as follows:

$$\frac{dI}{d\lambda} = -(\alpha_I + \vec{\alpha} \cdot \vec{p} - \epsilon_I)I, \quad (3)$$

$$\frac{d\vec{p}}{d\lambda} = -\vec{\alpha} + (\vec{\alpha} \cdot \vec{p})\vec{p} + \vec{p} \times \vec{p} + \vec{\epsilon} - \epsilon_I \vec{p}. \quad (4)$$

Here $\vec{\alpha} = (\alpha_Q, \alpha_U, \alpha_V)$ vector components are the invariant synchrotron absorptivities ($\alpha_{QUV} \equiv v\alpha_{v,QUV}$), $\vec{p} = (\rho_Q, \rho_U, \rho_V)$ are the invariant Faraday rotativities ($\rho_{QUV} \equiv v\rho_{v,QUV}$), $\vec{\epsilon} = (j_Q/I, j_U/I, j_V/I)$ are normalized invariant synchrotron polarized emissivities ($j_{QUV} \equiv j_{v,QUV}/v^2$), $\epsilon_I = j_I/I$ is a scalar quantity, and λ is the affine parameter. Equations are written down in the rest frame comoving with the fluid. Equation (3) means that the polarization of light colour impacts the absorption of total intensity via term $(\vec{\alpha} \cdot \vec{p})$. Notice that Faraday effects modify total intensity only via polarization vector \vec{p} .

Here, we are mostly interested in equation (4), which describes the motion of a polarization-representing point inside of the Poincaré sphere. Following Landi Degl’Innocenti & Landolfi (2004), the first term (i) $-\vec{\alpha}$ tends to align \vec{p} with $-\vec{\alpha}$, n.b. components of polarization vector \vec{p} can be negative or positive. This has a consequence for equation (3), $(\vec{\alpha} \cdot \vec{p})$ may act as negative absorptivity for Stokes \mathcal{I} . With (constant) term (i) alone, the fractional polarization grows with increasing λ . However, other terms may prevent this growth. The second term (ii) $(\vec{\alpha} \cdot \vec{p})\vec{p}$ is so called saturation term which prevents \vec{p} from crossing the Poincaré sphere. The importance of term (ii) increases as \vec{p} grows and results in polarization saturation. The third term (iii) in equation (4) describes precession of \vec{p} about \vec{p} or, in other

²The magnitude of the fractional circular polarization is expected to be smaller than fractional linear polarization. For a fixed frequency and $\Theta_e > 1$, the ratio of both polarization emissivities $j_V/j_Q \sim 2\Theta_e^{-1}$; hence if $|m| \sim 10$ per cent and $\Theta_e \approx 100$, $|v| \sim 0.1$ per cent.

Table 1. Electron heating parameters and polarimetric properties of simulation A.

ID	R_h	$\frac{\langle \dot{M} \rangle}{10^{-4}}$ ($M_\odot \text{ yr}^{-1}$)	i (deg)	$ m _{\text{net}}$ (%)		v_{net} (%)	
				Min	Max	Min	Max
A1	1	0.7	160	0.4	16	−0.2	0.1
			20	0.1	12.7	0	0.4
A10	10	1.13	160	1.3	12	−0.75	−0.12
			20	0.74	16.5	0.21	0.96
A100	100	1.9	160	0.8	9.9	−0.8	−0.15
			20	0.7	11.2	0.08	0.77
A200	200	2.24	160	0.35	7.6	−0.6	0.11
			20	0.5	6.4	0	0.5

– Four electron temperature parameters were used to simulate various modes of electron heating in collisionless plasma. Model characteristics for different electron models are shown in rows. Columns from left to right show: (1) model ID; (2) electron heating parameter (see text for description); (3) average mass accretion rate in physical units; (4 and 5) range of fractional linear polarization of near horizon emission measured using a time sequence of model images; (6 and 7) range of fractional circular polarization of near horizon emission measured using the same sequence of models.

words, Faraday rotation and conversion. Because Faraday rotation and conversion remove alignment between \vec{p} and $-\vec{\alpha}$, the presence of Faraday effects reduce polarization saturation and helps polarization to increase. The fourth and fifth terms in equation (4) act in the same way as terms (i) and (ii), $\vec{\epsilon}$ aligns \vec{p} with itself and $-\epsilon_I \vec{p}$ prevents saturation of fractional polarization.

Our full radiative transfer calculation are done using the numerical code `ipole`, which provides us with \vec{p} , $\vec{\alpha}$, and $\vec{\epsilon}$, along geodesics paths. We then examine the magnitude of all terms in the right-hand side of equation (4) and plasma and magnetic field properties, along the chosen light rays. By measuring the strength of each term, which controls polarization, we can associate it with location in the flow and specific components of the magnetic field or plasma conditions. Such polarization diagnostics is simplified because the full relativistic transfer in `ipole` includes parallel transport of polarization vector, hence the procedure allows us for discussion of fractional polarizations but not electric vector positions angle (EVPA), which is also modified due to parallel transport of polarization vector in strong gravity and Lorentz transformations from coordinate frame to frame comoving with the plasma. Notice that we set plasma comoving frame in a way so that one of the tetrad vectors is always aligned with magnetic field line in the plasma frame; hence in plasma frame $(j_U, \alpha_U, \rho_U) = 0$ by definition.

3 RESULTS

3.1 Effects of Faraday thickness

Our radiative transfer simulations assume four values of R_h parameter ranging between 1 and 200. Models with different electron temperature parameter have different mass scaling factors to produce total flux similar to that observed in astrophysical source at $f = 230$ GHz (in M87 that is about 0.5 Jy, Event Horizon Telescope Collaboration 2019a). Differences in the mass scaling results in a different accretion rates in physical units but the time dependence of accretion rate remains fixed. We report the averaged mass accretion rates obtained for each R_h parameter in Table 1. By changing overall mass and temperature of the simulations, we change the Faraday thickness of the model that affects the polarimetric images. The Faraday rotation

thickness is defined as $\tau_{\text{FR}} = \rho_V d\lambda$, where ρ_V is the Faraday rotativity, is expected to increase with R_h and accretion rate as $\tau_{\text{FR}} = \dot{M}^{3/2} R_h^2$ (see Mościbrodzka et al. 2017 for more details and Tsunetoe et al. 2020 for recent discussion of axi-symmetric GRMHD simulations). Faraday conversion thickness is also expected to increase with mass accretion rate, $\tau_{\text{FC}} \sim n_e B^2 \sim \dot{M}^2$. Notice that while Faraday rotation is sensitive to parallel field component, the conversion is larger in places where field lines are perpendicular to the line of sight.

In Fig. 4 we display total intensity and polarimetric images of the chosen snapshot ($t = 21\,150$ M) of model A for different values of R_h and two opposite, low viewing angles to present the appearance of the system from both sides. Rows in Fig. 4 correspond to the models with different electron temperature parameter, whose maps are shown Fig. 3. The polarimetric images of MADs are sensitive to the assumption of R_h parameter. In models with hot electrons in the accretion disc ($R_h = 1, 10$), the EVPA pattern is organized into a *vortex-like* structure. In models with sub-relativistic electrons in the accretion disc ($R_h = 100, 200$) the EVPA pattern becomes disorganized. The scrambling of the EVPA ticks is expected as a result of increasing Faraday depth in colder plasma as pointed out by Mościbrodzka et al. (2017). Indeed, we have measured that the Faraday rotation depth in our models is increasing with R_h and \dot{M} but the dependency is less steep function of these parameters (intensity weighted averaged $\langle \tau_{\text{FR}} \rangle_I = 8, 22, 87$, and 135 for $R_h = 1, 10, 100$, and 200 models, respectively). The enhanced Faraday rotations result in the significant decrease of the image net linear polarization via beam depolarization.

In Fig. 4, the maps of circular polarization highlight fractional circular polarization in the regions of relatively high total intensity. In contrast to linear polarization, the net fractional circular polarization increases with R_h . Note that although the resolved fractional circular polarization can be higher than 1 per cent, the v_{net} is less than unit for the given snapshot and all parameters. In models A1–A200, the total intensity weighted Faraday conversion depth range is $\langle \tau_{\text{FC}} \rangle_I = 0.02 - 0.1$ (Faraday conversion depth is proportional to the fraction of $|m|$ converted to v , Homan et al. 2009.).

It is also evident that models observed at opposite viewing angles show circular polarization of opposite signs. Noteworthy, the sign of the circular polarization in the lensing ring around the black hole shadow can be inverted with respect the net image circular polarization. The sign inversion is more visible in models with $R_h = 100$ and 200 (high Faraday thickness models), for both inclination angles.

3.2 Sign and strength of circular polarization in direct and lensed emission

GRMHD simulations and their polarization signal are complex. We first investigate the strength and sign of the circular polarization in the direct and lensed emission by decomposing the polarimetric images into far-side and near-side components.³ In the far-side/near-side images, the radiative transfer equations are integrated only below/above the mid-plane of the disc with respect to the observer.

We decompose different snapshot of model A200 into far and nearside images, the same model with Faraday conversion set to zero, $\rho_Q = 0$, and Faraday rotation set to zero, $\rho_V = 0$ are also shown (see the rightmost panels). Top panels in Fig. 5 show that Faraday conversion plays a key role in circular polarization formation

³Notice that fractional polarizations are not additive quantities so the plot is only indicative.

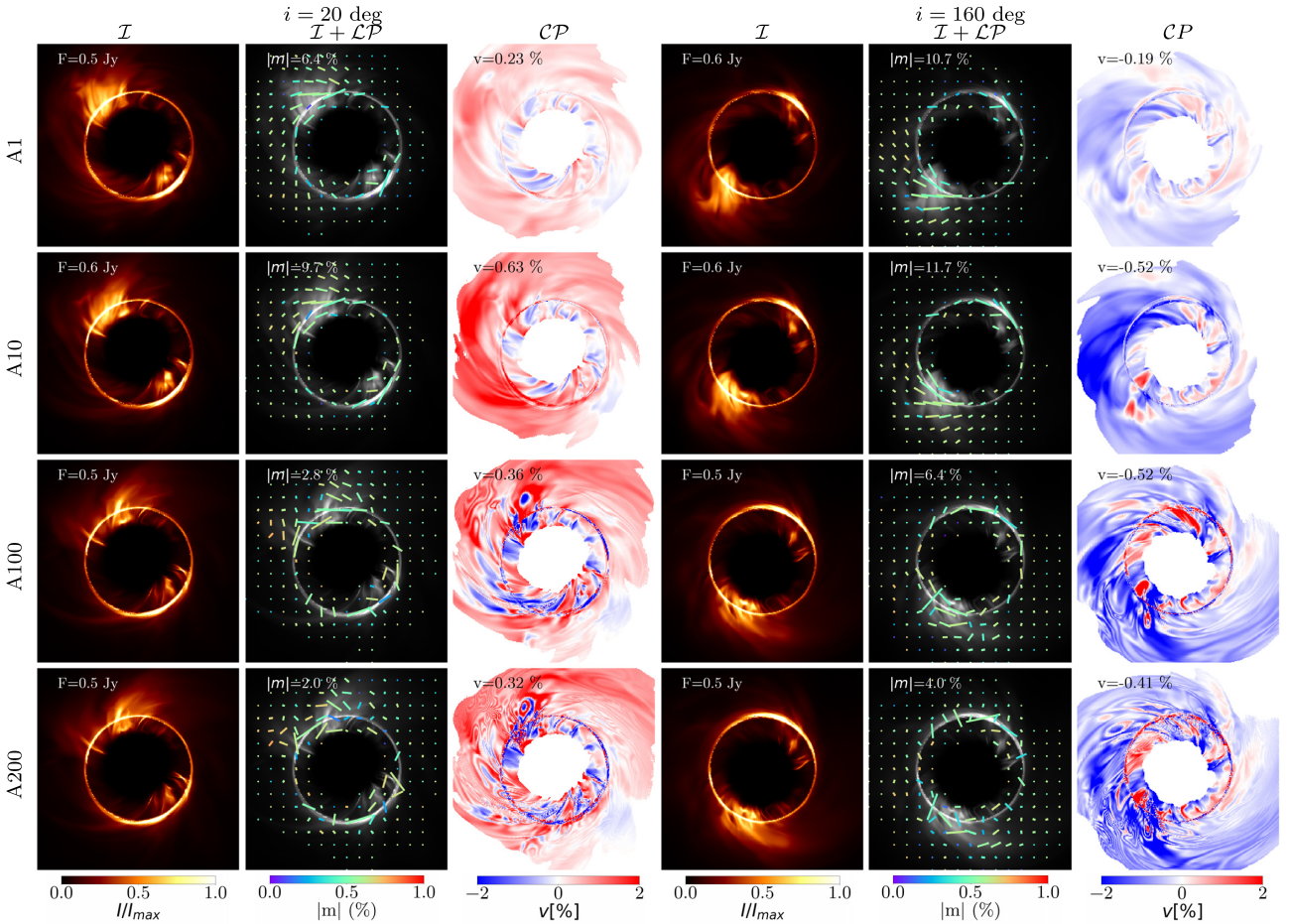


Figure 4. Polarimetric images of model A snapshot for different electron heating ratios (from top to bottom) and two close to face-on viewing angles (left-hand and right-hand panels). Panels from left to right display images of in total intensity (Stokes \mathcal{I}), linear polarimetric images (where total intensity is shown in grey scale in the background and polarization is shown in form of polarization ticks whose colour indicates the fractional polarization, length – total flux in polarization and polarization plane position angle – the EVPA), and circular polarization maps (using red-white-blue colour scale). In both linear and circular polarization images cuts has been made to omit displaying polarization regions where $I < 1$ per cent I_{\max} . Each panels field of view is 20×20 M.

even when Faraday rotation is not present. Without both Faraday effects the intrinsic circular polarization is significantly reduced. In contrast, without Faraday rotation alone, the circular polarization is significantly enhanced and has almost single handedness in the most of image regions. The latter suggest that the sign of the circular polarization is more sensitive to the direction of the rotation of the flow (Enßlin 2003) rather than polarity of the magnetic fields and Faraday rotation process (Beckert & Falcke 2002). In Appendix B, we discuss the impact of changing the global polarity of B-fields in the GRMHD simulation on polarimetric images. Interestingly, the results presented in Appendix B further support the idea that the Stokes \mathcal{QU} rotation and production of Stokes \mathcal{V} via conversion process mainly arises from rotation of plasma. Nevertheless, by comparing panels with full, near-side and far-side images and models with and without Faraday effects, we find that in the Faraday thicker flows, such as model A200, the details of the circular polarization depend on both Faraday effects: rotation and conversion. The nearside images of model with $\rho_V = 0$ and $\rho_V \neq 0$ suggest that Faraday rotation on the near-side is counteracting the increase of circular polarization. As a result only negative circular polarization emission regions below the equator visibly contribute to the final circular polarization map. These results can be understood as follows. The Faraday conversion changes Stokes \mathcal{U} together with its sign into

\mathcal{V} because $\rho_Q \sim n_e B^2 \sin^2 \theta$ (where θ is an angle between the light-wave vector and magnetic-field vector measured in the fluid frame) is always positive independently of the B-field sign. However, Faraday rotation does depend on the polarity of magnetic field, along the line of sight, since $\rho_V \sim n_e B \cos \theta$.⁴ Hence, when rays cross the near-side region the Faraday rotation changes the sign of \mathcal{U} because of overall opposite polarity of magnetic fields on the near-side compared to the far-side, hence the conversion process starts to subtract from the total \mathcal{V} rather than contribute to it. Finally, in Fig. 5, in all cases, the Stokes \mathcal{V} polarity inversion in the ring is present and it seems to be associated with the geometry of the light propagation.

Circular polarization produced in the Faraday thicker models has mostly one handedness and handedness inversion in the lensing ring. We check if similar effects are present in different realization of MAD models (B and C). In Fig. 6, we present examples of density maps, total intensity, and polarimetric images of models A, B, and C, all at $t \approx 19000$ M. At this time moment in each model, while accretion rate is similar, a different magnetic flux is accumulated on the horizon causing the dynamics of the flow near the horizon to be distinct.

⁴See Dexter 2016 for all Stokes synchrotron emissivities and rotativities used in our `ipole` code.

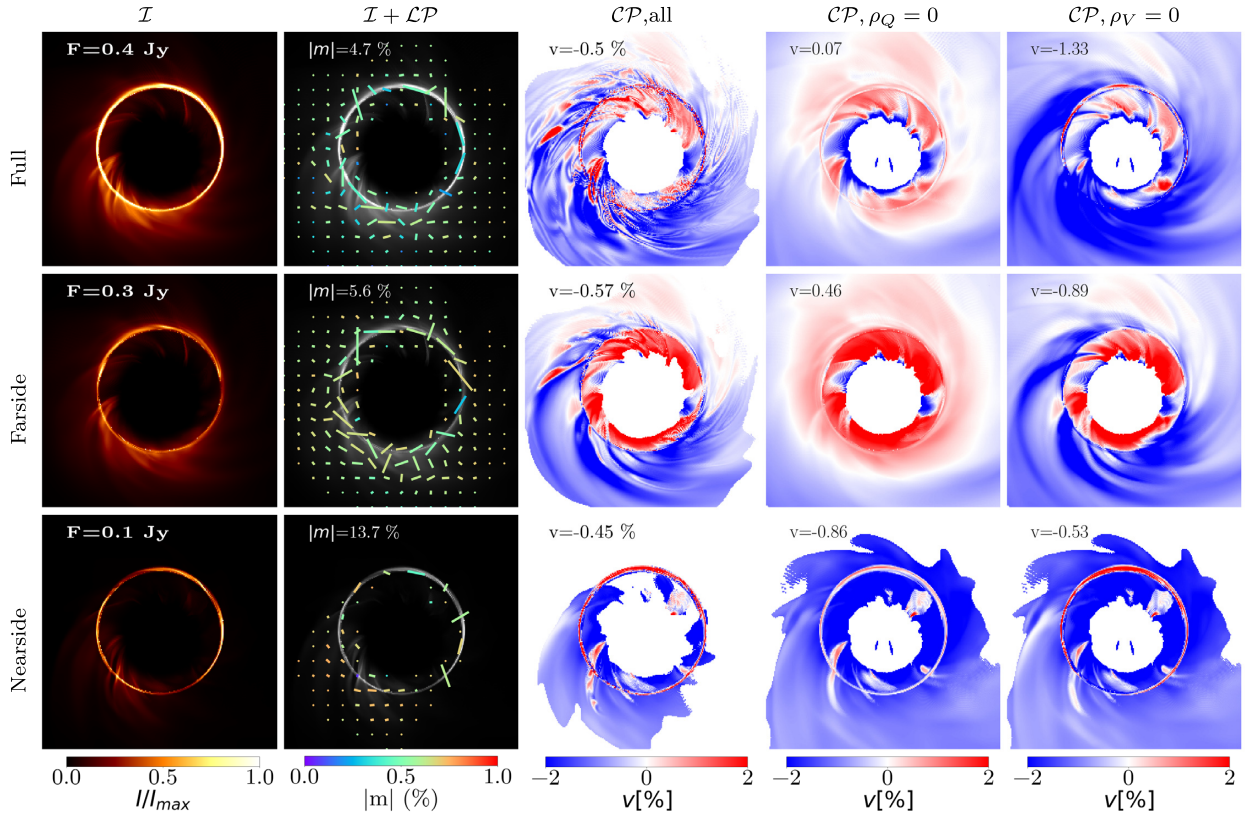


Figure 5. Decomposition of model A200 snapshot total intensity and polarimetric images (shown in top row) into far-side (middle row) and near-side contributions (bottom row). In far-side images, the radiative transfer equations are integrated until equatorial plane of the coordinate system, i.e. on the far-side of the black hole with respect to the observer. In the near-side images (bottom panels), the integration is done on the near-side of the black hole. Columns show total intensity, linear polarimetric images, and circular polarimetric images from left to right. The two rightmost circular polarimetric images assume no Faraday conversion, $\rho_Q = 0$ (total intensity and linear polarization remain unaffected by Faraday conversion) or no Faraday rotation $\rho_V = 0$ (for which only total intensity remains unaffected). All images are displayed in the same manner as in Fig. 4.

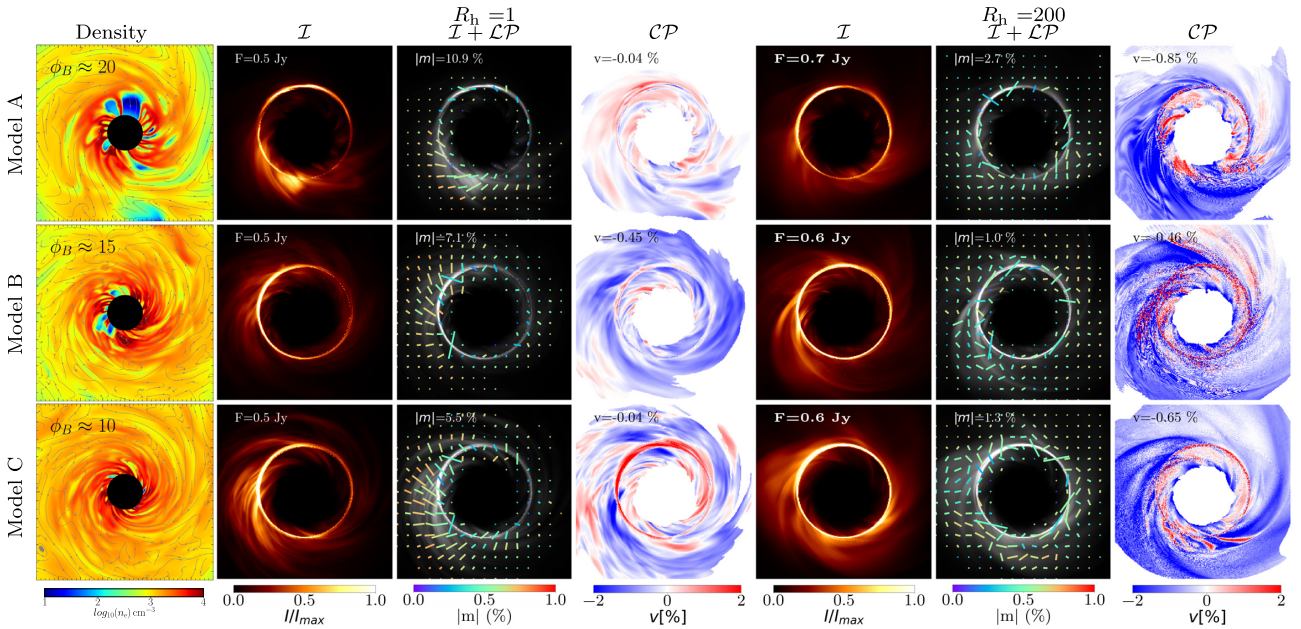


Figure 6. Polarimetric images of models A, B, and C (from top to bottom) for $R_h = 1$ and 200 and nearly face-on viewing angle, $i = 160 \text{ deg}$. The left-most panels show maps of plasma density distribution at the equatorial plane together with projected magnetic field lines. Second/fifth, third/sixth, and fourth/seventh panels display the total intensity (Stokes \mathcal{I}), linear and circular polarimetric images. Images are displayed in the same manner as in Fig. 4.

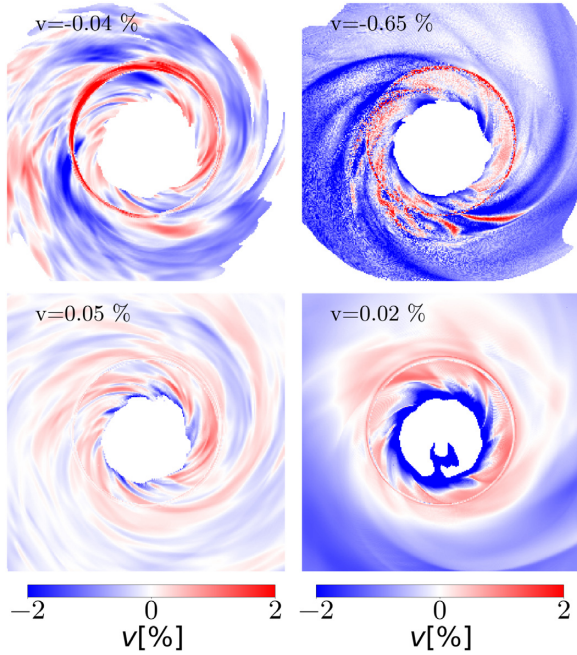


Figure 7. Circular polarization maps of model C1 (left-hand panels) and C200 (right-hand panels) by performing the full radiative transfer (top panels) and with $\rho_Q = 0$ (i.e. no Faraday conversion, bottom panels). The inversion of the ring polarity disappears when Faraday conversion effects are not included.

The stronger magnetic barrier, created by extended magnetosphere in the polar regions (visible in Fig 2, top left panel), makes the inner disc in equatorial plane more inhomogeneous in azimuthal direction. Evidently, in models A and B, the streams of matter have to overpass stronger magnetic barrier compared to model C. While the streams in model A and B are not purely radial but slightly bend, the structure of density in C model indicates stronger toroidal component of magnetic fields. In Fig. 6, we show the corresponding polarimetric maps of models A, B, and C for $R_h = 1$ and $R_h = 200$. The model B and C behaviour as a function of R_h is similar to model A. Linear polarization maps become disorganized with increasing R_h parameter. Circular polarization maps of model B and C display similar features to their counterpart model A, as expected. The net circular polarization is negative and small but increases with R_h parameter. All models show polarity inversion in the lensing ring when $R_h = 200$. Notice that in model C, the ring inversion for $R_h = 1$.

In Fig. 7, we show circular polarization maps of model C1 and C200 (model C with $R_h = 1$ and 200 in analogy to models A1 and A200). These two snapshots have similar conversion thickness ($\langle \tau_{FC} \rangle_I = 0.1$ and 0.17 in models C1 and C200, respectively) but different rotation thickness ($\langle \tau_{FR} \rangle_I = 0.49$ and 322 in models C1 and C200, respectively). Again, Faraday conversion play a key role in the production of circular polarization in the direct and in the lensed emission. The polarity inversion effect in the lensing ring seems to be robust in all three realizations of MADs as long as Faraday conversion thickness is significant.

3.3 Polarization variability versus underlying magnetic fields and plasma conditions

Does the variability of the linear and circular polarization reflect variability in the underlying magnetic field or mass accretion rate?

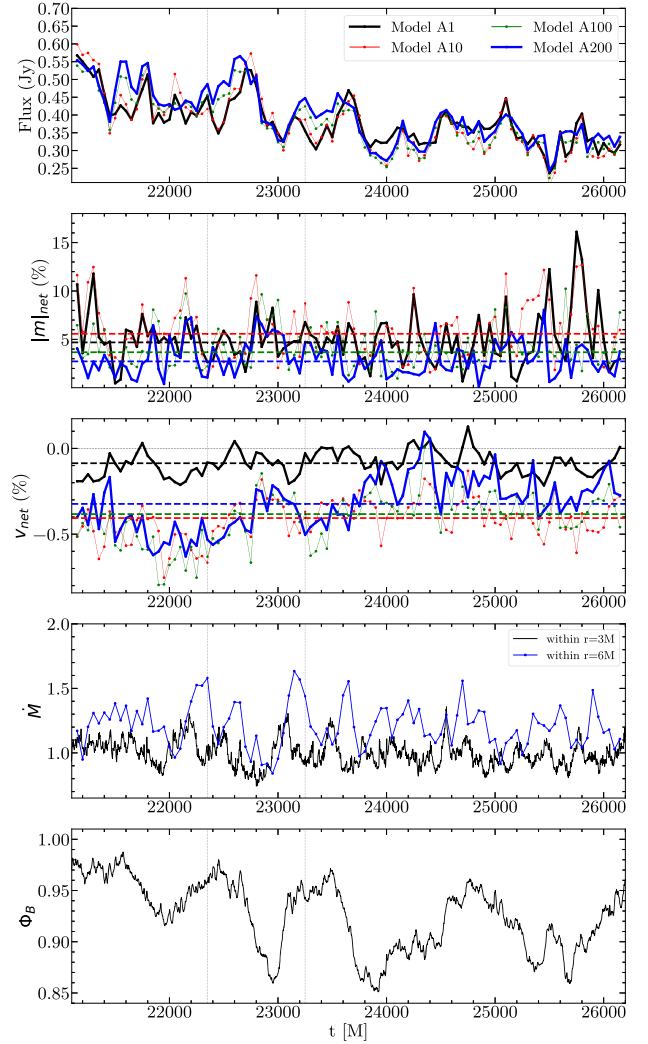


Figure 8. Time variability in models A1, A10, A100, and A200 (models with different electron temperatures are colour coded). Three top panels display time variations in total flux, net fractional linear polarization $|m|_{\text{net}}$, and the net fractional circular polarization v_{net} for observer at $i = 160$ deg. In panels with $|m|_{\text{net}}$ and v_{net} , the horizontal lines mark corresponding median polarizations. Two bottom panels display the normalized to unity mass accretion rate through the event horizon and the magnetic field flux accumulated at the event horizon (in code units). Two mass accretion rates are averaged within 3 and within 6 M. The thin vertical lines mark time are moments shown in Figs 11 and 12.

To further investigate the physical origin of circular polarization and its variations as a function of time, we analyse a longer sequence of model A snapshots ($\Delta t = 5000$ M) corresponding to 5 yr of M87 core evolution.

In Fig. 8, we show models A1 through A200 total intensity fluxes, net fractional linear ($|m|_{\text{net}}$), and net circular (v_{net}) polarization integrated over entire images, mass accretion rate, and magnetic flux threading horizon as a function of time. The latter two are the global physical parameters of the model that one is interested to constrain using observables so they are shown for a comparison. Horizontal lines in panels with fractional polarizations mark median values of fractional polarizations. Results are shown for runs with viewing angle of 160 deg but the images at 20 deg display similar properties. In Table 1, we report ranges of net fractional linear and circular polarizations integrated over all images within the considered time

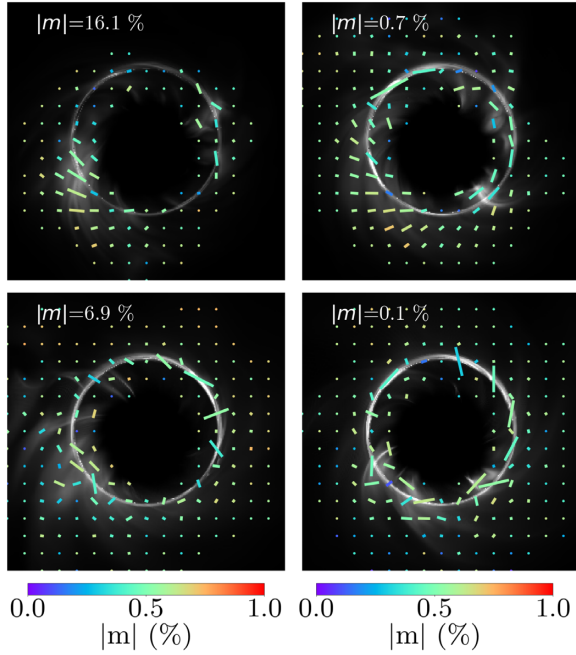


Figure 9. Examples of linear polarimetric images of model A1 (top panels) and A200 (lower panels), which display relatively high (left-hand panels) and low (right-hand panels) net linear polarizations. Total intensity and polarizations are displayed in the same manner as in Fig. 4. Snapshot times are: $t = 25\,750$ M (top left), $t = 25\,200$ M (top right), $t = 22\,150$ M (bottom left), and $t = 24\,850$ M (bottom right).

period for both viewing angles. Models with higher R_h parameter tend to display lower net linear polarization and higher (in the absolute sense) net circular polarization. In our runs, the magnitude of net circular polarization remains rather small, $v_{\text{net}} < 1$ per cent, with median value of $v_{\text{net}} = -0.05$ per cent in model A1 and median value of $v_{\text{net}} \approx -0.4$ per cent in A10, A100, and A200 runs. For all displayed models, the sign of the net circular polarization is most of the time constant for the assumed viewing angle. The sign flips of v_{net} occur slightly more frequently in model A1 in comparison to other models (where other models have higher Faraday thickness for rotations and conversions).

In Fig. 9, we show examples of linear polarization images of two models (with thoroughly different Faraday thicknesses) A1 and A200 ($i = 160$ deg) when $|m|_{\text{net}}$ is relatively high (well above the median value) or extremely low ($|m|_{\text{net}} < 1$ per cent). All images display complex polarimetric structures due to interplay of different effects. In frames with high-net-linear polarization, larger patches of highly polarized emission regions are present. Images with low-net-linear polarization either display a few smaller regions of organized polarization in different directions or are scrambled by Faraday rotation effect, both resulting in low $|m|_{\text{net}}$. In models with higher Faraday thickness (A200), the patches with coherent high polarization are also possible and so the high-net polarization is. In Fig. 10, we show a few examples of model A1 and A200 circular polarization maps with relatively high- and low-net circular polarizations. Those with high absolute v_{net} often show stronger features.

The connections between the observed linear/circular polarization and physical parameters, such as mass accretion rate and magnetic flux at the horizon are not immediately obvious (see Fig. 8, bottom panels). We have examined all images in our time sequence and no

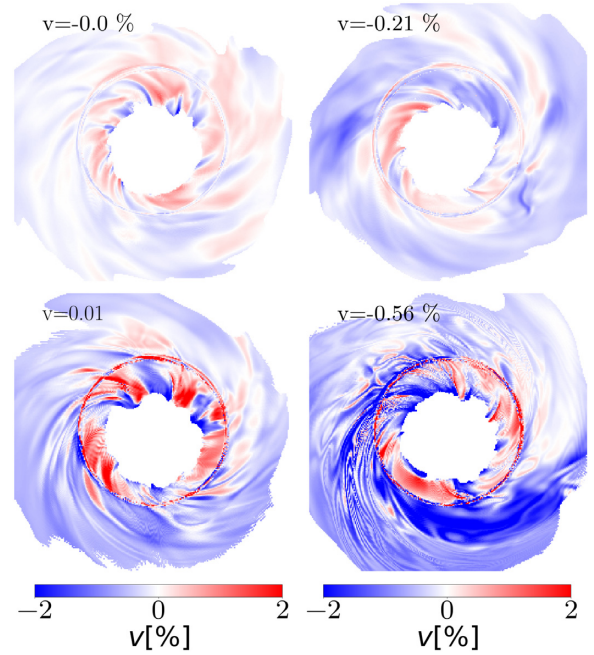


Figure 10. Examples of circular polarimetric images of model A1 (top panels) and model A200 (bottom panels), which display relatively high- (left-hand panels) and low- (right-hand panels) net circular polarizations. The circular polarizations are displayed in the same manner as in Fig. 4. Snapshot times are: $t = 24\,300$ M (top left), $t = 23\,100$ M (top right), $t = 24\,350$ M (bottom left), and $t = 22\,400$ M (bottom right). Notice that snapshots chosen for display here are different from those shown in Fig. 9.

characteristic linear polarization pattern associated with enhanced accretion rate or magnetic field flux near the event horizon was found. Instead, we found examples of model A1 and A200 images with similar linear polarization patterns and net polarizations but accretion rates different by a factor of two.

Circular polarization maps, with fractional polarizations smaller compared to linear polarization, are likely more sensitive to changes in the plasma and magnetic field conditions. Using method outlined in Section 2.3, we examine the origin of circular (and linear) polarization in two example snapshots of models A200, which show high absolute circular polarizations (these times are $t = 22\,350$ M and $t = 23\,250$ M marked in Fig. 8 with thin vertical lines).

In Figs 11 and 12, we show the chosen polarimetric images (left-hand panels) and various quantities, along a single light ray towards the highly circularly polarized emission region (marked with a circle in the right-hand panels). Figs 11 and 12 (panels with $dp_Q/d\lambda$, $dp_U/d\lambda$, $dp_V/d\lambda$) show that the linear polarization along the chosen ray is produced by intrinsic emission away from the equatorial plane and strongly modified by Faraday rotation in the flow mid-plane (position of the equator is marked as vertical dotted line in each panel), where temperature of plasma is cooler (even sub-relativistic). The self-absorption effects for linear and circular polarization are negligible. Circular polarization is predominantly produced in the conversion process in the disc material, where the toroidal-radial magnetic field components is stronger (above 1 Gauss). The latter is observed in both examples. In Fig. 11, the sign of Stokes \mathcal{U} changes sign at the equator due to Faraday rotation, hence the Stokes \mathcal{V} slightly decreases above the equatorial plane. This finding is consistent with the results presented in Section 3.2.

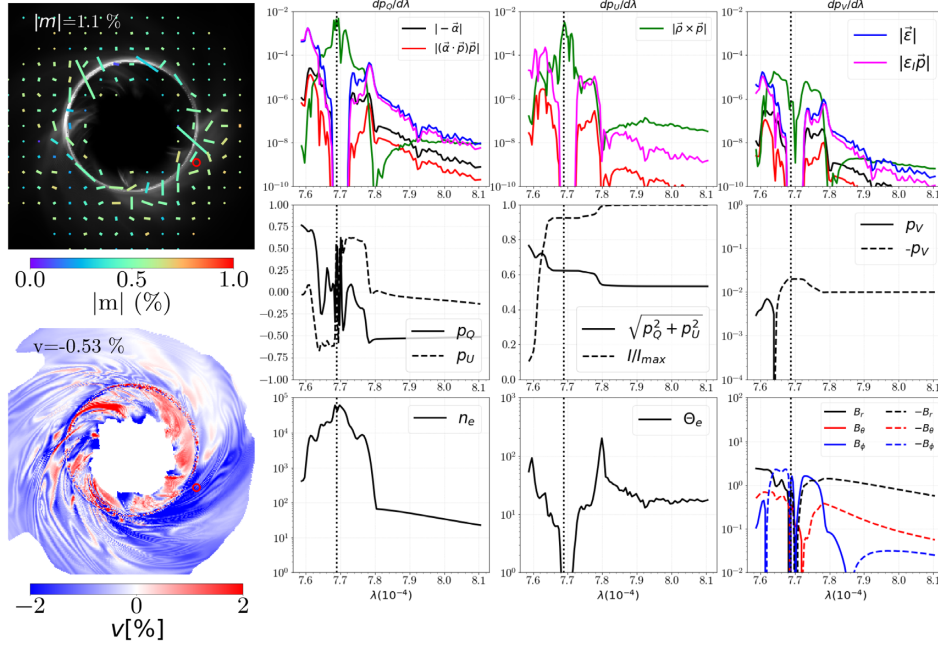


Figure 11. Polarimetric images (left-hand panels) and polarization diagnostic plot (right-hand panels) showing profiles of various quantities, along a single geodesic line marked as a red circle in the left-hand panel. We display model A200 snapshot that has relatively high circular polarization. In the right-hand panels, we follow integration details from the geodesics point where the total intensity \mathcal{I} is equal 10 per cent of the ray final intensity until radius of 8 M (within a region where most of the radiation is generated). Vertical dotted line marks passage of light ray through the equatorial plane. First row: equation (4) terms (i) through (v) for each of the Stokes parameters \mathcal{Q} , \mathcal{U} , and \mathcal{V} (shown in columns from left to right; notice that labels displayed in each panel are valid for all other panels in this row). Second row: fractional polarizations in all Stokes parameters and normalized total intensity. Third row: plasma number density (cm^{-3}), dimensionless electron temperature ($\Theta_e = k_B T_e / m_e c^2$), and the three magnetic field components (measured in the coordinate frame in units of Gauss). Here, one can notice that the mid-plane of the disc is dominated by Faraday effect. Linear polarization is mostly produced away from the mid-plane and scrambled by Faraday rotation. Majority of circular polarization is produced below the disc mid-plane where toroidal-radial component of magnetic fields dominates.

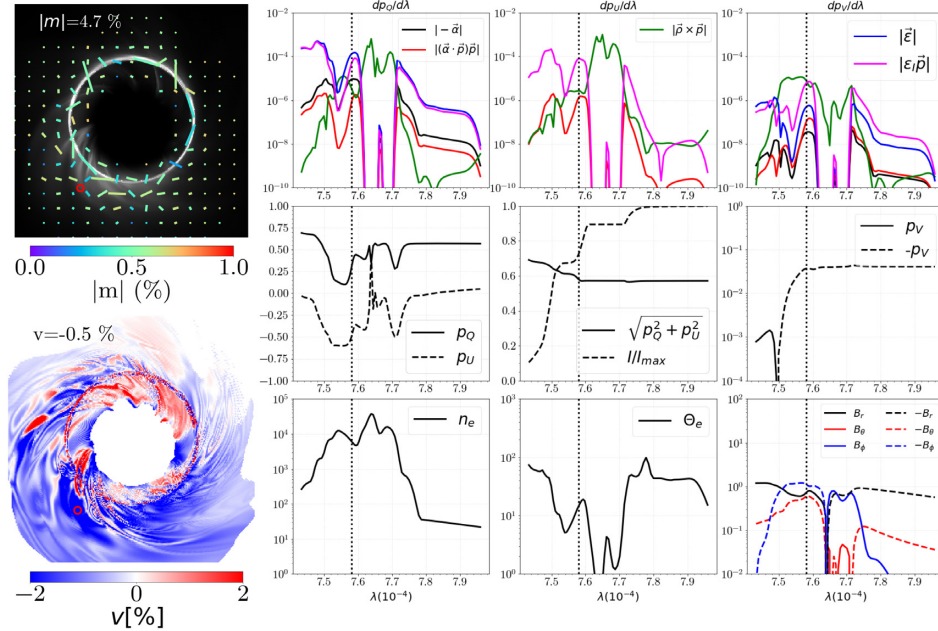


Figure 12. Polarimetric images (left-hand panels) and polarization diagnostic plot (right-hand panels) for another highly circularly polarized snapshot of model A200. All panels display various quantities in the same fashion as in Fig. 11. Here, the polarization is formed in a similar way as in case shown in Fig. 11.

4 SUMMARY

We have examined simulated polarimetric images of accreting black hole produced by ray-tracing high resolution simulation of magnetically dominated accretion flow. We arrive at the following general conclusions:

(i) The magnitude of the resolved $|m|$ and v in black hole images removes degeneracy between parameters of the models for electron temperatures. Models with lower/higher R_h parameter display stronger/weaker $|m|$ and weaker/stronger v . This finding is consistent with the idea of Mościbrodzka et al. (2017), where we pointed out that parameter R_h controls Faraday depth of the models, which may cause linear depolarization and lead to enhanced circular polarization.

(ii) We do not attempt to fit our models to M87 black hole observations, but rather use the source as an example to point out observational signatures of dynamical magnetic fields around this type of objects when accretion flow is in MAD state. Nevertheless, models with low-net linear polarization ($|m|_{\text{net}} \sim 1 - 3.7$ per cent), or rather high R_h parameter, are favoured by M87 observations (Kuo et al. 2014, Event Horizon Telescope Collaboration 2021a). Using the same model scoring procedure as the one introduced in Event Horizon Telescope Collaboration 2021b, we have found that our model A200 is consistent with polarimetric observations of M87 reported by the Event Horizon Telescope. If indeed M87 black hole is surrounded by MAD with $R_h = 200$ parameter then the expected resolved circular polarization around the black hole could be as large as a few per cent. However, our prediction is inconsistent with results of Tsunetoe et al. 2020, who based on their best-bet model, predicted circular polarization of the M87 core to be larger than 10 per cent. The difference may be due to different GRMHD setups (2D versus 3D models studied here or different model magnetization).

(iii) Our findings about the circular polarization handedness are consistent with the idea of Enßlin (2003) who associates it with the direction of rotation. If this is indeed the case, M87 core should have negative/positive circular polarization in case if the source is rotating in the clock-wise/counter-clock-wise direction on the sky.

(iv) We discover the polarity inversion in circular polarimetric images of black hole shadow. The polarity inversion in the lensing ring is also associated with the stronger Faraday conversion in regions on the nearside of the black hole. Detection of the polarity inversion in Stokes V in emission region in M87 could provide evidence that the ring visible in the EHT observations (Event Horizon Telescope Collaboration 2019a) is produced near event horizon rather than being a feature of the forward jet (see e.g. models in appendix A in Davelaar et al. 2019 or Kawashima et al. 2020). The frequency of $f = 230$ GHz may be an optimal frequency for such observation because Faraday conversion decreases with observing frequency as f^{-3} , which will decrease fractional circular polarization at higher frequencies (see e.g. images in Appendix C). At $f < 230$ GHz, on the other hand, the near horizon emission is rather obscured by the synchrotron photosphere so no such inversion effects would be visible.

(v) We find that variations in the circular polarization maps reflect the variations in the underlying magnetic field strength around it. These variations are best highlighted in models with high Faraday conversion thickness. The Faraday conversion strength is proportional to B_{\perp} component, along the line of sight. Hence, for our low-viewing angles (nearly face-on), Faraday rotation would be enhanced in regions where toroidal (or other component of field that is perpendicular to the line of sight in a given setup) field is significant. The Faraday conversion seems to be highlighting polarity of magnetic fields on one side of the disc where polarity is more or less the same so it results in increased v_{net} and images with uniform polarity. In contrast to resolved quantities, the $|m|_{\text{net}}$ and v_{net} do not

correlate with physical parameters of the accreting system, such as accretion rate or magnetic field flux at the black hole event horizon.

(vi) Finally, the effects described in this paper may not be universal to all possible accretion models and viewing angles. Investigating circular polarization magnitude and variations in different accretion models (e.g. Standard and Normal Evolution instead of MADs) around black hole with different spin values or models with non-thermal electrons are all possible directions for the future research.

ACKNOWLEDGEMENTS

The authors thank Daniel Palumbo, Alejandra Jimenez-Rosales, Hector Olivares, and Jesse Vos for useful comments and suggestions, which significantly improved the quality of the manuscript. MM acknowledges support by the The Dutch Research Council grant no. OCENW.KLEIN.113. AJ acknowledges support by the grant no. 2019/35/B/ST9/04000 from the Polish National Science Center, and using computational resources of the Interdisciplinary Centre for Mathematical and Computational Modelling in Warsaw through grant Gb79-9, and the PL-Grid through the grant plggrb4. The paper uses public code `ipole` available at [www.github.com/moscibrodzka/aipole](https://github.com/moscibrodzka/aipole) (Mościbrodzka & Gammie 2018).

DATA AVAILABILITY

The data underlying this article will be shared on reasonable request to the corresponding author.

REFERENCES

- Beckert T., Falcke H., 2002, *A&A*, 388, 1106
- Beckwith K., Hawley J. F., Krolik J. H., 2008, *ApJ*, 678, 1180
- Blandford R. D., Payne D. G., 1982, *MNRAS*, 199, 883
- Blandford R. D., Znajek R. L., 1977, *MNRAS*, 179, 433
- Bower G. C., Falcke H., Backer D. C., 1999, *ApJ*, 523, L29
- Bower G. C., Falcke H., Mellon R. R., 2002, *ApJ*, 578, L103
- Bower G. C. et al., 2018, *ApJ*, 868, 101
- Broderick A. E., Loeb A., 2009, *ApJ*, 697, 1164
- Brunthaler A., Bower G. C., Falcke H., 2006, *A&A*, 451, 845
- Chael A. A., Johnson M. D., Narayan R., Doeleman S. S., Wardle J. F. C., Bouman K. L., 2016, *ApJ*, 829, 11
- Chael A., Narayan R., Johnson M. D., 2019, *MNRAS*, 486, 2873
- Connors P. A., Piran T., Stark R. F., 1980, *ApJ*, 235, 224
- Davelaar J. et al., 2019, *A&A*, 632, A2
- Dexter J., 2016, *MNRAS*, 462, 115
- Dexter J., Agol E., Fragile P. C., McKinney J. C., 2010, *ApJ*, 717, 1092
- Dexter J., McKinney J. C., Agol E., 2012, *MNRAS*, 421, 1517
- Enßlin T. A., 2003, *A&A*, 401, 499
- Event Horizon Telescope Collaboration, 2019a, *ApJ*, 875, L4
- Event Horizon Telescope Collaboration, 2019b, *ApJ*, 875, L5
- Event Horizon Telescope Collaboration, 2021a, *ApJ*, 910, L12
- Event Horizon Telescope Collaboration, 2021b, *ApJ*, 910, L13
- Fishbone L. G., Moncrief V., 1976, *ApJ*, 207, 962
- Gammie C. F., McKinney J. C., Tóth G., 2003, *ApJ*, 589, 444
- Goddi C. et al., 2021, *ApJ*, 910, L14
- Himwich E., Johnson M. D., Lupsasca A., Strominger A., 2020, *Phys. Rev. D*, 101, 084020
- Homan D. C., Lister M. L., 2006, *AJ*, 131, 1262
- Homan D. C., Wardle J. F. C., 1999, *AJ*, 118, 1942
- Homan D. C., Lister M. L., Aller H. D., Aller M. F., Wardle J. F. C., 2009, *ApJ*, 696, 328
- Ishihara H., Takahashi M., Tomimatsu A., 1988, *Phys. Rev. D*, 38, 472
- Janiuk A., Sukova P., Palit I., 2018, *ApJ*, 868, 68
- Jiménez-Rosales A., Dexter J., 2018, *MNRAS*, 478, 1875
- Kawashima T., Toma K., Kino M., Akiyama K., Nakamura M., Moriyama K., 2020, *ApJ*, 909, 168

- Kuo C. Y. et al., 2014, *ApJ*, 783, L33
- Landi Degl’Innocenti E., Landolfi M., 2004, *Polarization in Spectral Lines*. University of Firenze, Firenze, Italy; Arcetri Observatory, Firenze, Italy. ASTROPHYSICS AND SPACE LIBRARY Volume 307 Kluwer Academic Publishers, Dordrecht
- Marrone D. P., Moran J. M., Zhao J.-H., Rao R., 2007, *ApJ*, 654, L57
- McKinney J. C., Tchekhovskoy A., Blandford R. D., 2012, *MNRAS*, 423, 3083
- Mizuta A., Ebisuzaki T., Tajima T., Nagataki S., 2018, *MNRAS*, 479, 2534
- Mościbrodzka M., Gammie C. F., 2018, *MNRAS*, 475, 43
- Mościbrodzka M., Falcke H., Shiokawa H., 2016, *A&A*, 586, A38
- Mościbrodzka M., Dexter J., Davelaar J., Falcke H., 2017, *MNRAS*, 468, 2214
- Muñoz D. J., Marrone D. P., Moran J. M., Rao R., 2012, *ApJ*, 745, 115
- Narayan R., Igumenshchev I. V., Abramowicz M. A., 2003, *PASJ*, 55, L69
- Noble S. C., Gammie C. F., McKinney J. C., Del Zanna L., 2006, *ApJ*, 641, 626
- Proga D., Begelman M. C., 2003, *ApJ*, 592, 767
- Rayner D. P., Norris R. P., Sault R. J., 2000, *MNRAS*, 319, 484
- Ressler S. M., White C. J., Quataert E., Stone J. M., 2020, *ApJ*, 896, L6
- Sapountzis K., Janiuk A., 2019, *ApJ*, 873, 12
- Tsunetoe Y., Mineshige S., Ohsuga K., Kawashima T., Akiyama K., 2020, *PASJ*, 72, 32
- Wardle J. F. C., Homan D. C., Ojha R., Roberts D. H., 1998, *Nature*, 395, 457
- Yuan F., Narayan R., 2014, *ARA&A*, 52, 529

APPENDIX A: SLOW-LIGHT VERSUS FAST-LIGHT POLARIZED RADIATIVE TRANSFER MODEL

In the radiative transfer simulations, we neglect the light travel-time delay effects and post-process each simulation snapshot separately,

as if photons propagated at infinite speed (so called ‘fast-light’ approach). Here, we explicitly show how well this commonly used approximation holds for total intensity and light linear and circular polarizations.

We carry out several radiative transfer simulations and compare light curves and images generated using the fast-light approach to those generated by propagating photons through time-evolving simulation (referred as to ‘slow-light’). To carry out the tests, we utilize another 3D GRMHD simulation of a torus where the cadence of the dump files is $\Delta t = 1$ M (the simulation is SANE with black hole spin parameter $a_* = 0.9375$). High cadence is needed for accurate interpolations of fluid variables between the time snapshots (Dexter et al. 2010). All fast-light and slow-light transfer calculations are carried out in modified Kerr–Schild coordinates.

In Fig. A1, in three top panels, we show temporal behaviour of total flux and fractional linear and circular polarizations as measured by a distant observer at three chosen viewing angles. The time is shown in units of M, where $t = 0$ M corresponds to about $t = 1500$ M in evolution of the torus, hence the turbulence in the torus is well evolved for this test. The two types of light curves shown correspond to results of slow- and fast-light models. The difference in total flux is less than 10 per cent. This result is consistent with results and discussion by Dexter et al. 2010 who compared slow- and fast-light approach in unpolarized radiative transfer models. Notice that, here we do not see the time shift between two light curves that is visible in figs 9 and 10 of Dexter et al. (2010) because the light curves produced in slow and fast-light calculations are aligned in time by maximizing mean normalized cross-correlation between the individual frames used to construct the light curves. In Fig. A1, in three bottom panels, we show these normalized cross-correlations

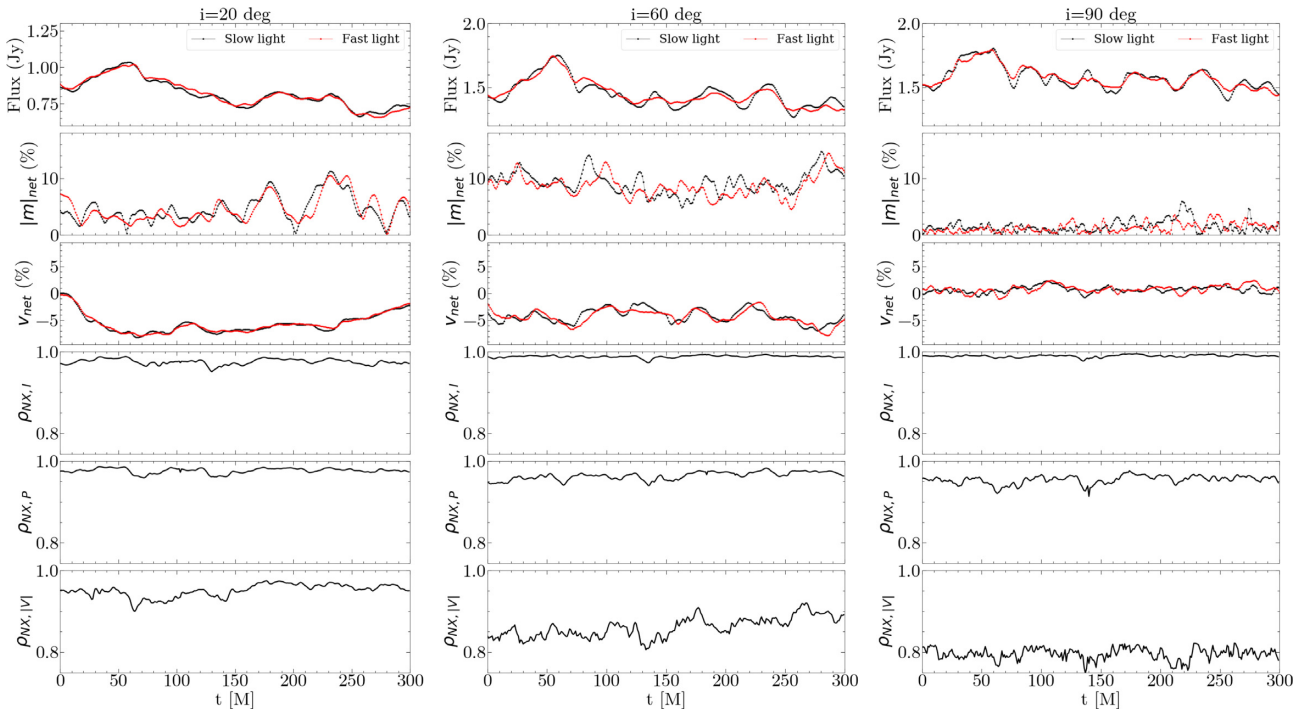


Figure A1. Temporal behaviour of observables calculated using slow-light and fast-light approximation for three viewing angles ($i = 20, 60$, and 90 deg from left to right). Top three panels display flux, fractional linear, and circular polarization as a function of time. Bottom three panels display normalized cross-correlation between images computed using slow-light and fast-light approximation. Cross-correlation coefficient is computed separately for total intensity images, $\rho_{NX,I}$, linear polarimetric images (where $P = \sqrt{Q^2 + U^2}$), $\rho_{NX,P}$ and circular polarimetric images, $\rho_{NX,V}$. The slow-light and fast-light light curves in the top three panels are aligned so that the cross-correlation coefficients in the bottom panels have maximum mean value within the shown time interval.

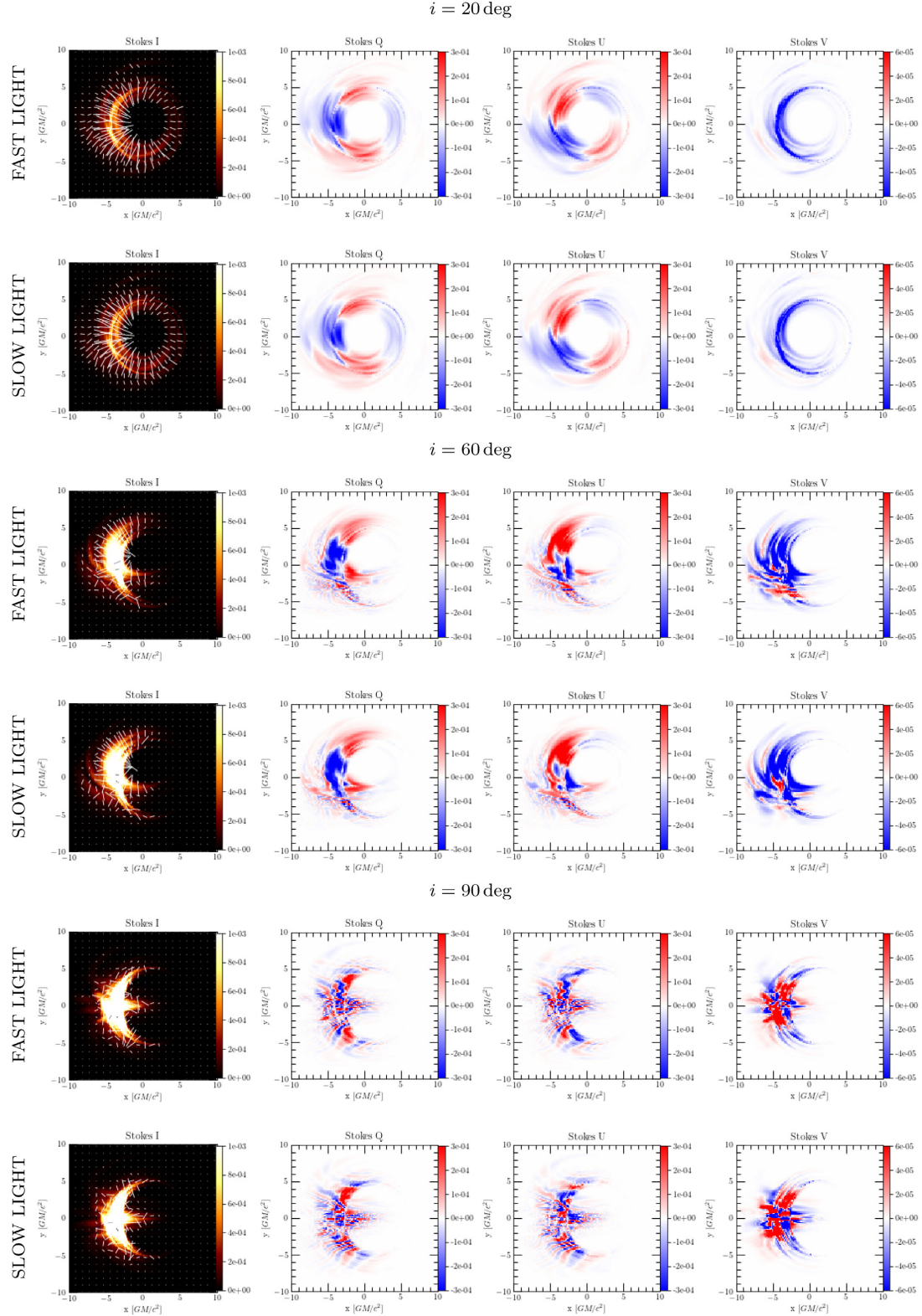


Figure A2. Examples of Stokes images constructed using slow-light and fast-light radiative transfer models for three chosen viewing angles. For these examples, the normalized cross-correlations between slow- and fast-light polarimetric images, $(\rho_{NX, I}, \rho_{NX, P}, \rho_{NX, |V|})$ are (0.98, 0.98, 0.96) for $i = 20 \text{ deg}$, (0.98, 0.97, 0.9) for $i = 60 \text{ deg}$ and (0.99, 0.96, 0.8) for $i = 90 \text{ deg}$.

between slow- and fast-light images, computed separately for Stokes \mathcal{I} , Stokes $\mathcal{P} \equiv \sqrt{Q^2 + U^2}$, and absolute value of Stokes \mathcal{V} . The cross-correlation coefficients, ρ_{NX} , are calculated using `nxcorr` function in `eht-imaging` library (Chael et al. 2016). The images computed in slow light model are highly correlated with those from fast-light approximation both in total intensity and both polarizations. In Fig. A2, we show examples of fast and slow light images in all Stokes parameters. Images with more scrambled polarization (e.g. with viewing angle of $i = 90$ deg), the cross-correlation for \mathcal{P} and $|\mathcal{V}|$ is slightly worse compared to Stokes \mathcal{I} , because polarization maps are more sensitive to small changes in the fluid conditions. What follows, one should be cautious when interpreting any observed time variations in Stokes \mathcal{Q} and \mathcal{U} with fast-light models that have scrambled linear polarization (where scrambled polarization can be due to either turbulence or higher Faraday depth).

The slow-light models are computationally far more expensive compared to the fast-light models. Given small differences between two approaches, we choose the cheaper approach to predict radiative properties of the long duration simulations.

APPENDIX B: B-FIELD POLARITY IN GRMHD SIMULATIONS

We start GRMHD simulations with a single loop of magnetic field inside of a torus. The polarity of the loop is set arbitrarily because the GRMHD model evolution is insensitive to the polarity of the magnetic fields. However, the polarized radiative transfer equations in the plasma frame are not symmetric when changing the B-field sign, which may result in different polarimetric images.

The asymmetry of polarized radiative transfer with respect to B-field polarity becomes evident when examining the properties of equation (4). Let's consider two cases. In the first case, let's assume that there are no Faraday effects ($\vec{\rho} \times \vec{p} = 0$). Then Stokes \mathcal{Q} (linear polarization) will not depend on B-field polarity but the sign of Stokes \mathcal{V} will reflect B-field polarity. This is because the sign of the normalized synchrotron emissivity ϵ_Q , absorptivity α_Q , as well as $\vec{\alpha} \cdot \vec{p}$ do not depend on the sign of B-field, while the sign of ϵ_V

and α_V do. Notice that in this first case, the magnitude of circular polarization remains unchanged when changing the sign of the B-field. In the second case, we consider full radiative transfer model with all Faraday effects included. In this case, the polarity of the magnetic field does make a difference to both linear and circular polarization and, to a very small degree, can affect Stokes \mathcal{I} . To understand this effect one has to understand the behaviour of $(\vec{\rho} \times \vec{p})$ when the sign of B-field changes. It is useful to write this term separately for Stokes \mathcal{Q} , \mathcal{U} , \mathcal{V} :

$$(\vec{\rho} \times \vec{p})_Q = -\rho_V p_U, \quad (\text{B1})$$

$$(\vec{\rho} \times \vec{p})_U = \rho_V p_Q - \rho_Q p_V, \quad (\text{B2})$$

$$(\vec{\rho} \times \vec{p})_V = \rho_Q p_U, \quad (\text{B3})$$

where sign of Faraday conversion coefficient, ρ_Q , does not depend on B-field sign while sign of Faraday rotativity, ρ_V , does. It is evident that the change in B-field sign will cause change in the Stokes \mathcal{Q} evolution via Faraday rotation (only one term in equation 4 will change sign), which will be followed by change in evolution of Stokes \mathcal{U} and then \mathcal{V} , via Faraday conversion. In this case, we also expect to see small difference in Stokes \mathcal{I} because the magnitude of term $\vec{\alpha} \cdot \vec{p}$ in equation (3) can be altered.

In Fig. B1, we show that our numerical scheme is in agreement with the above considerations. We show a snapshot of model A200 (the same one as shown in Fig. 5) computed with and without the inversion of B-field sign. We present two aforementioned cases in which emission and absorption only and emission, absorption and Faraday effects are included in the computation. As expected in the first case, the inversion of B-fields makes no difference for Stokes \mathcal{I} , \mathcal{Q} , \mathcal{U} and the magnitude of Stokes \mathcal{V} but the sign of Stokes \mathcal{V} is reversed. The first case additionally demonstrates that our numerical scheme is accurate. In the second case, in model with Faraday effects included (lower panels in Fig. B1), the linear and circular polarizations changed between models of different B-field polarity. Interestingly, in maps with circular polarization, only regions that are Faraday-thin (within the photon ring in the central regions of the

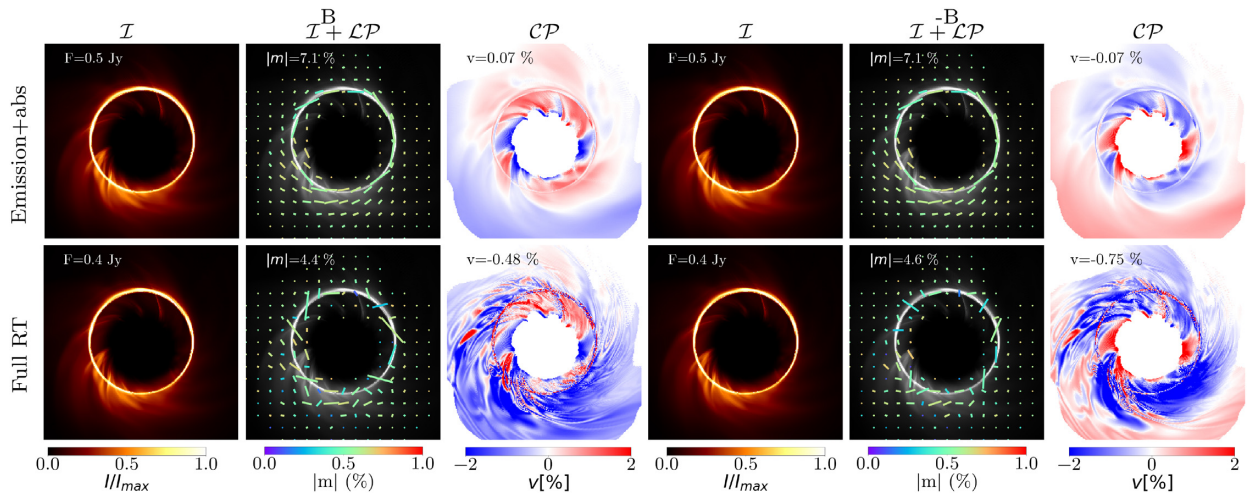


Figure B1. Impact of the global magnetic field polarity on the linear and circular polarization maps of model A200. Top panels show the maps computed without Faraday effects accounting only for emission and self-absorption effects. As expected linear polarization remains unaffected with circular polarization maps swap sign when magnetic field sign is reversed. Bottom panels show the same model when solving full radiative transfer (RT) equations, including Faraday effects, as expected a significant change is visible in both linear and circular polarization maps.

frame and in the outer regions of the frame) swap the polarity, while Faraday-thick regions in the most bright part of the frame – retain the Stokes \mathcal{V} signature. These results support the idea that the handedness of Stokes \mathcal{V} is more sensitive to the direction of the rotation of the flow (or in other words: the handedness of the magnetic field helix), rather than the polarity of the magnetic fields (Enßlin 2003).

APPENDIX C: OBSERVING FREQUENCY EFFECTS

In our analysis, we study polarimetric maps at $f = 230$ GHz corresponding to the EHT observing frequency. Future observations by this instrument will image M87 black hole near horizon emission at $f = 345$ GHz. Planned space VLBI projects will aim to observe black hole horizons at even higher frequencies $f = 690$ GHz. At these higher frequencies, the images of black holes are expected to have higher resolution enabling to resolve better the finer structures around the black hole shadow, such as e.g. the lensing ring. Here, we recalculate model A200 images at two higher frequencies to investigate which frequency is optimal for circular polarization observations or how observations at different frequencies can complement each other.

In Fig. C1, we show example snapshot of model A200 at $f = 230, 345$, and 690 GHz. The Faraday conversion is decreasing with observing frequency as f^{-3} and so the fractional circular polarization decreases significantly for higher energies. The inversion of polarization in the lensed emission is hardly visible already at 345 GHz. However, also the Faraday rotations decrease with the frequency and one can observe the intrinsic polarization patterns, which are not scrambled and reflect better the geometry of magnetic fields in the emission region.

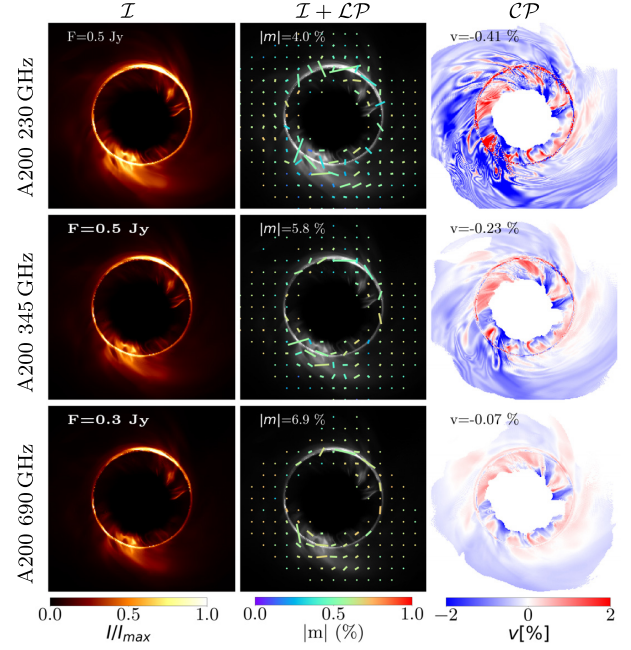


Figure C1. Frequency dependency of polarimetric images of model A200 observed at $i = 160$ deg. The time moment is the same as shown in Fig. 4 and images are displayed in the same manner as in Fig. 4.

This paper has been typeset from a \LaTeX file prepared by the author.